A&A 627, A80 (2019)
https://doi.org/10.1051/0004-6361/201834948

Astronomy & Astrophysics

Deuterated methanol toward NGC 7538-IRS1⋆

J. Ospina-Zamudio[1], C. Favre[1,2], M. Kounkel[3], L.-H. Xu[4,⋆], J. Neill[5], B. Lefloch[1], A. Faure[1], E. Bergin[5], D. Fedele[2], and L. Hartmann[5]

[1] Université Grenoble Alpes, CNRS, IPAG, 38000 Grenoble, France
e-mail: juan-david.ospina-zamudio@univ-grenoble-alpes.fr
[2] INAF – Osservatorio Astrofisico di Arcetri, Largo E. Fermi 5, 50125 Florence, Italy
[3] Department of Physics and Astronomy, Western Washington University, 516 High St, Bellingham, WA 98225, USA
[4] Centre for Laser, Atomic, and Molecular Sciences (CLAMS), Department of Physics, University of New Brunswick, PO Box 5050, Saint John, NB, Canada
[5] Department of Astronomy, University of Michigan, 1085 South University Avenue, Ann Arbor, Michigan 48109, USA

Received 21 December 2018 / Accepted 15 May 2019

ABSTRACT

We investigate the deuteration of methanol towards the high-mass star-forming region NGC 7538-IRS1. We carried out a multi-transition study of CH_3OH, $^{13}CH_3OH$, and the deuterated flavors, CH_2DOH and CH_3OD, between 1.0 and 1.4 mm with the IRAM-30 m antenna. In total, 34 $^{13}CH_3OH$, 13 CH_2DOH lines and 20 CH_3OD lines spanning a wide range of upper-state energies (E_{up}) were detected. From the detected transitions, we estimate that the measured D/H does not exceed 1%, with a measured CH_2DOH/CH_3OH and CH_3OD/CH_3OH of about $(32 \pm 8) \times 10^{-4}$ and $(10 \pm 4) \times 10^{-4}$, respectively. This finding is consistent with the hypothesis of a short-timescale formation during the pre-stellar phase. We find a relative abundance CH_2DOH/CH_3OD ratio of 3.2 ± 1.5. This result is consistent with a statistical deuteration. We cannot exclude H/D exchanges between water and methanol if water deuteration is of the order 0.1%, as suggested by recent *Herschel* observations.

Key words. ISM: molecules – ISM: abundances – radio lines: ISM – astrochemistry – ISM: individual objects: NGC 7538

1. Introduction

Observational studies of deuterated molecules are powerful ways to probe the chemical and physical evolution of star-forming regions. Indeed, many of the organic species that are abundant constituents of molecular clouds are synthesized in the cold prestellar phase (see Caselli & Ceccarelli 2012, for a review). At low temperatures, the difference in zero-point energy between deuterated molecules and their hydrogenated counterparts (about 1000 K for methanol and its singly deuterated flavors, Nandi et al. 2019) makes it possible for deuterated species to be formed with significantly higher relative abundances than the elemental D/H ratio ($\sim 10^{-5}$, see e.g., Ceccarelli et al. 2007, 2014; Caselli & Ceccarelli 2012). These enhanced abundance ratios can be preserved as the protostar heats the gas to temperatures large enough (≥100 K) to evaporate the ice mantles. Thus, studies of molecular D/H ratios can provide strong insight into the physical history of star-forming regions along with information on the chemical routes through which the molecular content is formed. Deuterium fractionation in low-mass star-forming regions has been the subject of significant study (e.g., see Roberts et al. 2002; Parise et al. 2006; Ratajczak et al. 2011; Jørgensen et al. 2018). These sources have shown remarkably high enhancements of deuterated molecules, including even doubly and triply deuterated species (e.g., ND_3, CD_3OH), which in some cases occur at abundances 12–13 orders of magnitude higher than elemental abundance would suggest (Lis et al. 2002; Parise et al. 2002, 2004). Regarding high-mass star-forming regions, only a few observations of deuterated molecules have been performed so far (e.g., Jacq et al. 1993; Ratajczak et al. 2011; Peng et al. 2012; Neill et al. 2013a,b), the best studied high-mass source of deuterated molecules being the Orion KL nebula. Low levels of fractionation are typically observed, consistent with molecular formation at higher temperatures; alternatively, warm gas-phase chemistry could alter the D/H ratio in high-mass regions during the post-evaporative phase. Interestingly enough, from chemical modeling using experimental kinetic data, Faure et al. (2015a) suggested that the D/H ratio measured in Orion-KL might not be representative of the original mantles due to deuterium exchanges between water and methanol in interstellar ices during the warm-up phase. The study of the abundance ratio of the deuterated isotopologs of methanol (CH_3OD/CH_2DOH) could give access to the initial deuteration of water ices before the warm-up phase sets in. Nonetheless, taking into account the limited number of observations of deuterated species in high-mass star-forming regions, the extent to which the D/H ratios observed toward Orion KL are representative of high-mass source chemistry is uncertain. Bøgelund et al. (2018) recently reported low deuteration levels of methanol towards the HMSFR NGC6334 I, with typical values in the range of 0.01–1% for both CH_2DOH and CH_3OD. Large uncertainties on the column densities of a factor of 4–10 depending on the species remain however, which prevent any robust conclusions on the CH_2DOH/CH_3OD ratio and the initial ice composition. Further observations of a sample of high-mass sources are thus required for comparison between sources and for improving our understanding of the chemistry that creates organic molecules with significant deuterium fractionation (in particular, the roles of grain-surface and gas-phase reactions).

⋆ This paper is dedicated to the memory of our dear colleague, Dr. Li-Hong Xu, who recently passed away.

In this study, we investigate the D/H ratio for methanol (CH_3OH, CH_2DOH, and CH_3OD) towards the high-mass star-forming region NGC 7538-IRS1 ($L = 1.3 \times 10^5$ $L_\odot$, $d = 2.8$ kpc, $M \sim 30$ $M_\odot$, see Bisschop et al. 2007; Beuther et al. 2012), which is known to harbor high abundances of organic molecules, including methanol (e.g., Bisschop et al. 2007; Wirström et al. 2011). Results are given in Sect. 3 and discussed in Sect. 4.

2. Observations and data reduction

The data were acquired with the IRAM 30 m telescope on 2013 December 5, 6, and 10 towards NGC 7538-IRS1 with a single pointing ($\alpha_{J2000} = 23^h13^m45\overset{s}{.}5$, $\delta_{J2000} = +61°28'12\overset{''}{.}0$). The v_{LSR} was −57 km s^{-1}. The observations were taken in position-switching mode, using a reference for the OFF position at [−600″, 0″]. The EMIR receiver at 1 mm was used in connection with the Fourier transform spectrometer (FTS) as backend, providing a spectral resolution of 195 kHz. The spectral resolution was subsequently degraded to 780 KHz, which corresponds to about 1 km s^{-1}, in order to improve the signal-to-noise ratio (S/N) of the data. The following frequency ranges were covered: 212.6–220.4 GHz, 228.3–236.0 GHz, 243.5–251.3 GHz, 251.5–259.3 GHz, 259.3–267.0 GHz, and 267.2–274.9 GHz. The half-power beam sizes are 10″ and 12″ for observations at 250 and 212 GHz, respectively.

The data were reduced using the CLASS90 package from the GILDAS software[1]. The spectra are reported in this study in main beam temperature units, T_{MB}, given by $T_{MB} = \frac{\eta_f}{\eta_{MB}} \times T_A^*$, where T_A^* is the antenna temperature, η_f the forward efficiency (η_f = 94, 92 and 87 at 210, 230 and 274 GHz, respectively), and η_{MB} the main beam efficiency (η_{MB} = 63, 59, 49 at 210, 230 and 274 GHz, respectively[2]). Finally, the data presented some spurs along with standing waves, which have been removed during the data reduction. In this paper, we focus on methanol and its deuterated flavors.

The spectroscopic parameters of the targeted lines are given in Appendix A (see Tables A.1–A.4). More specifically, we used the spectroscopic data parameters[3] from Xu & Hougen (1995a,b), Xu & Lovas (1997), Xu et al. (2008), and Müller et al. (2004) for CH_3OH. The parameters for CH_2DOH come from Pearson et al. (2012) and those for $^{13}CH_3OH$ are from Xu & Lovas (1997), Xu et al. (1996, 2008, 2014). Regarding CH_3OD, we used the same unpublished data as Neill et al. (2013b) used for analyzing the HIFI/*Herschel* observations of Orion-KL. Nonetheless, the CH_3OD partition functions we use in the present study (see also, Walsh et al. 2000) are given in Appendix B. Finally, collisional rates are assumed to be identical to those of CH_3OH and taken from Rabli & Flower (2010). This point is addressed in more detail in Sect. 3.3

3. Results and analysis

3.1. Detected lines

We detect several bright lines covering a wide range of upper energy levels: 34 $^{13}CH_3OH$ lines with E_{up} spanning from 23 to 397 K; 13 CH_2DOH lines with E_{up} spanning from 25 to 94 K; and 20 CH_3OD lines (10 lines for both A- and E-forms) with E_{up} spanning from 19 to 271 K. The observational line parameters of the clearly detected transitions are summarized in Tables A.1–A.4.

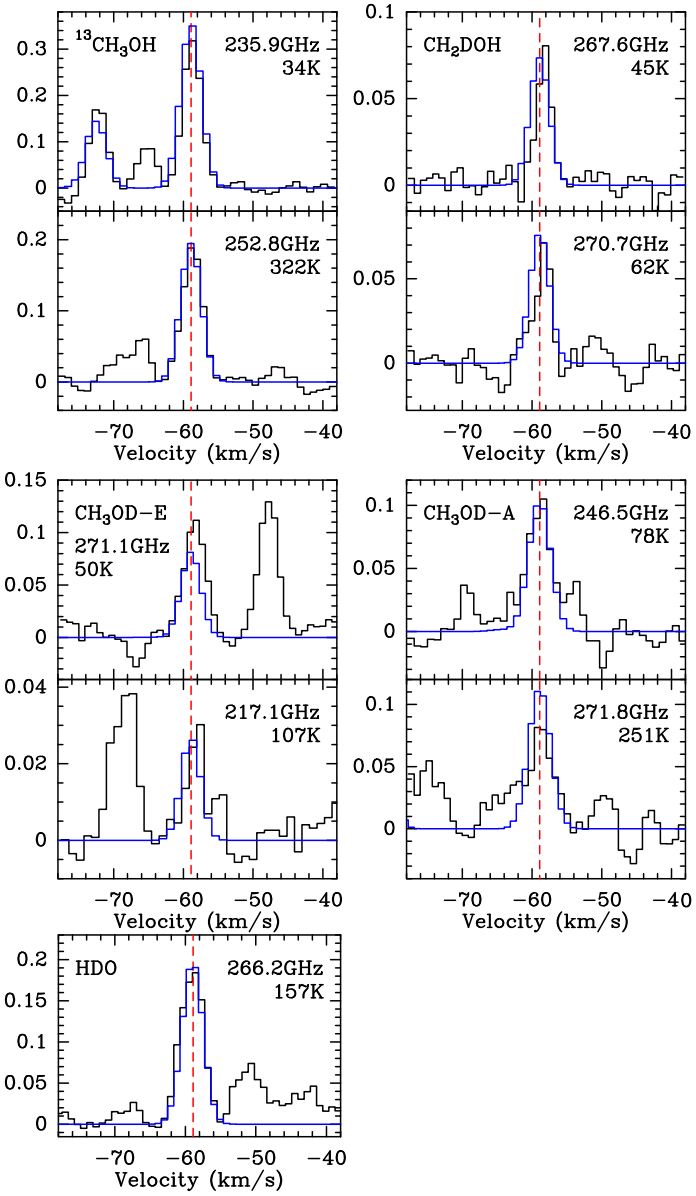

Fig. 1. Montage of detected transitions of methanol ^{13}C isotopolog and deuterated forms along with that of the detected HDO line. Intensities are expressed in units of T_{mb}. Our LTE modeling is displayed in blue. The red dashed line marks the peak velocity of methanol transitions $v_{LSR} = -58.9$ km s^{-1}.

The lines profiles are well fitted by a single Gaussian profile with a little scatter on the fitted full width at half maximum (mean $\Delta v = 3.4 \pm 0.7$ km s^{-1}) and the peak intensity velocity (mean $v_{LSR} = 58.6 \pm 0.6$ km s^{-1}). We note that the scatter on the peak velocity lies within 1 element of spectral resolution (1 km s^{-1}), which makes us confident as to the line assignations. In addition, if we take into account the pointing uncertainties (typically 1″–2″), the observed scatter in emission velocity peak is consistent with the large velocity gradient observed within the source by Beuther et al. (2012, and their Fig. 8). Figure 1 shows a montage of two detected transitions probing different excitation energies of $^{13}CH_3OH$, CH_2DOH, and CH_3OD (A and E) along

[1] http://www.iram.fr/IRAMFR/GILDAS/
[2] See http://www.iram.es/IRAMES/mainWiki/Iram30mEfficiencies
[3] The spectroscopic data parameters are available at the Cologne Database for Molecular Spectroscopy catalog (CDMS; Müller et al. 2005) and/or at the JPL catalog (Pickett et al. 1998).

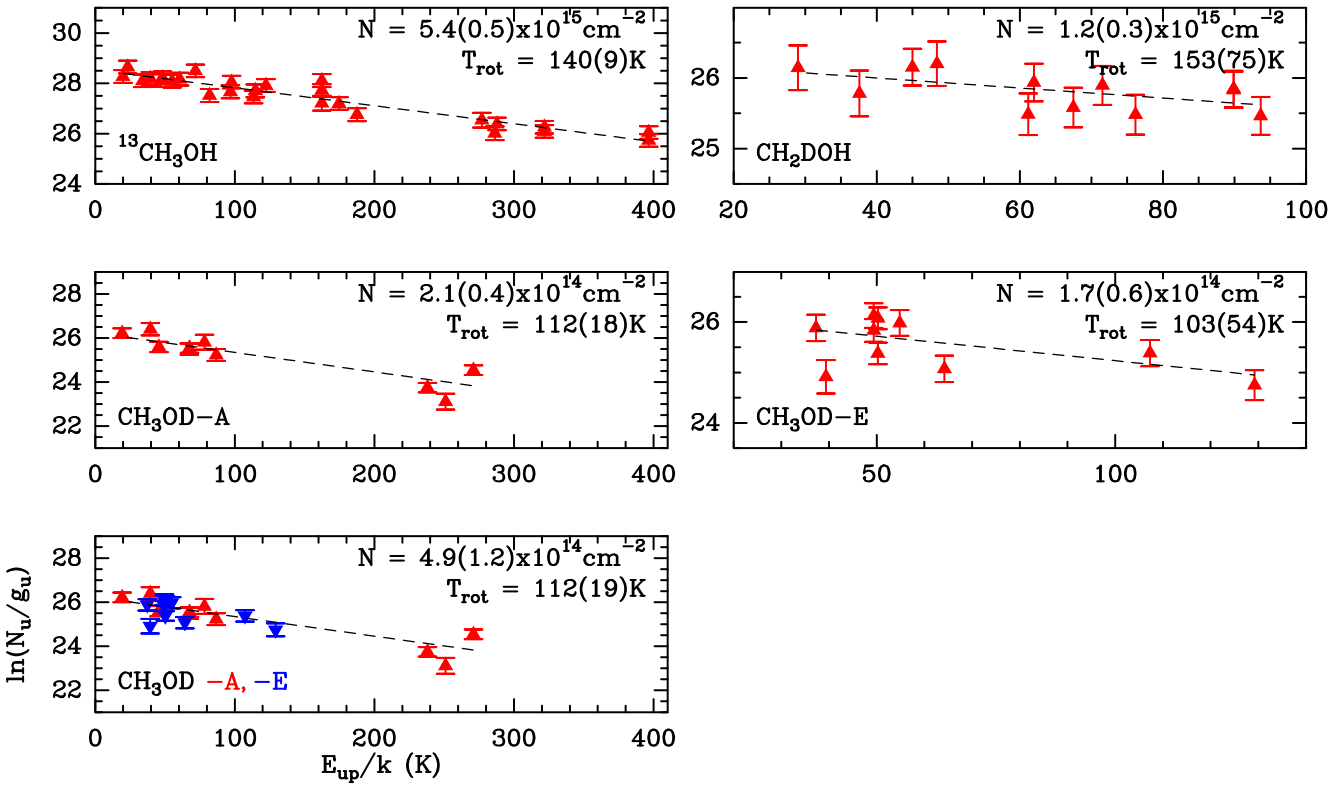

Fig. 2. Population diagram analysis of the ^{13}C-methanol and the deuterated forms. A size of 3.8″ was adopted for the emitting region. In the analysis we separate the methanol E-form from the A-form. However, as shown in the bottom left panel, their respective SLEDs are consistent with one another. Finally, please note that the y-range varies from plot to plot.

with our local thermodynamical equilibrium (LTE) modeling. In addition, Fig. 1 also displays the spectrum of the $2_{2,0}$–$3_{1,3}$ transition of deuterated water which is also detected in our survey. Finally, Figs. C.1–C.3 display a montage of all the detected transitions associated with the $^{13}CH_3OH$, CH_2DOH, and CH_3OD species along with our LTE modeling.

3.2. Local thermodynamical equilibrium analysis

The physical properties (excitation temperature, column densities) of the methanol species were obtained from a population diagram analysis of their spectral line energy distributions (SLEDs). In the present study, we assume a source size of 3.8″, corresponding to the ice evaporation region (see Bisschop et al. 2007). The derived column densities are therefore determined and given for a source size of 3.8″. We estimate the line opacities, under LTE conditions following Goldsmith & Langer (1999). We conclude that the $^{13}CH_3OH$, CH_2DOH, and CH_3OD emissions are optically thin with $\tau \leqslant 0.03$. We note that most of the transitions associated with the main methanol isotopolog are optically thick with $\tau(CH_3OH) \geq 1$. As a consequence, we cannot determine the excitation temperature and column density of the $^{12}CH_3OH$ with sufficiently accurate precision. We therefore exclude the analysis of the $^{12}CH_3OH$ for the present study. The resulting physical properties are summarised in Table 1.

Figure 2 shows the population diagrams that are all well fitted by a single rotational temperature. More specifically, the population diagram analysis of $^{13}CH_3OH$ yields $N(^{13}CH_3OH) = (5.4 \pm 0.5) \times 10^{15}$ cm^{-2} and $T_{\rm rot} = 140 \pm 9$ K. Assuming a $^{12}C/^{13}C$ elemental abundance ratio of 70 for the local ISM (Wilson 1999), we determine the methanol column density $N(CH_3OH) = (3.8 \pm 0.4) \times 10^{17}$ cm^{-2}. Regarding CH_2DOH, we estimate a rotational temperature similar to that of ^{13}C methanol, $T_{\rm rot} = 153 \pm 75$ K, and a column density $N(CH_2DOH)$ of $(1.2 \pm 0.3) \times 10^{15}$ cm^{-2}. For CH_3OD we derive a lower rotational temperature of $T_{\rm rot} = 103 \pm 54$ K (112 ± 18 K) for both the E- and A-forms. Nonetheless, within the error bars, the derived rotational temperatures for the deuterated methanol flavors are in agreement with that of the ^{13}C isotopolog. The derived column densities of both E- and CH_3OD-A are comparable with $N(CH_3OD\text{-E}) = (1.7 \pm 0.6) \times 10^{14}$ cm^{-2} and $N(CH_3OD\text{-A}) = (2.1 \pm 0.4) \times 10^{14}$ cm^{-2}, which results in a total CH_3OD column density, $N(CH_3OD)$, of $(3.8 \pm 1.0) \times 10^{14}$ cm^{-2}. We note that the computed total CH_3OD column density is commensurate within the error bars to that found if we treat both substates (E- and A-) simultaneously (see Fig. 2).

Table 1. Physical properties of methanol isotopologs: rotational temperature and column density.

Species	$T_{\rm rot}$ (K)	N (10^{14} cm^{-2})
$^{13}CH_3OH$	140 ± 9	54 ± 5
CH_2DOH	153 ± 75	12 ± 3
CH_3OD-E	103 ± 54	1.7 ± 0.6
CH_3OD-A	112 ± 18	2.1 ± 0.4

Notes. A source size of 3.8″ was adopted.

3.3. Nonlocal thermodynamic equilibrium analysis

The present section aims to verify whether the apparent LTE distribution of the CH_3OD targeted transitions is consistent

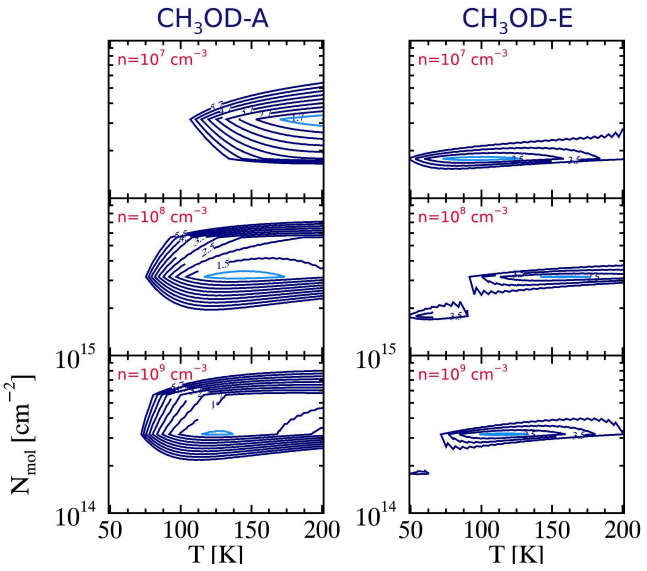

Fig. 3. CH_3OD-A (*left column*) and CH_3OD-E (*right column*) χ^2 distributions as computed with RADEX for $n = 10^7$, 10^8 and 10^9 cm^{-3}. The minimum χ^2 is displayed in cyan.

with nonLTE conditions along with the derived densities and temperatures.

For this purpose we combined the (unpublished) spectroscopic data of CH_3OD (energy levels and radiative rates) with the collisional rate coefficients computed by Rabli & Flower (2010) for the rotational excitation of CH_3OH by H_2. We assumed that the -OH H/D substitution has a negligible impact on the scattering dynamics (the change in reduced mass is only 0.2%). The coupled statistical equilibrium–radiative transfer equations were then solved using the RADEX code (van der Tak et al. 2007).

Assuming a source size of 3.8″ and a line width of 4 km s^{-1}, we ran a grid of models for the following gas densities $n = 10^7$, 10^8, and 10^9 cm^{-3} with the kinetic temperature varying from 20 to 200 K and the CH_3OD column density lying between 1×10^{10} and 1×10^{19} cm^{-2}. We then compared the observed and modeled LGV CH_3OD-A and CH_3OD-E integrated fluxes by the mean of the χ^2. The computed results and minimized χ^2 distributions are shown in Fig. 3.

There is no common solution for both E- and A-species with a density of 10^7 cm^{-3}. A common region of minimum χ^2 in the parameter space (N,T) is found for a density in the range 10^8–10^9 cm^{-3}. The latter is commensurate with the one derived by Beuther et al. (2012) from PdBI observations as well as that derived by Bisschop et al. (2007) from *James Clerk Maxwell* Telescope (JCMT) observations. Our best fits are obtained for a CH_3OD column density of about $\simeq 3 \times 10^{14}$ cm^{-2} and a temperature of 100–150 K, both consistent with our LTE analysis.

4. Discussion

4.1. D/H in methanol

As can be seen in Table 2, the fractionation degree of singly deuterated methanol is low in NGC 7538-IRS1, with relative abundance values of 0.1% (taking into account the statistical ratio for the -CH_3 functional group). Such values are similar to those reported towards other HMSRs like Orion KL. Thanks to the numerous detected lines for both CH_2DOH and CH_3OD, the relative abundance between the two deuterated flavors is determined with good accuracy, and is found to be equal to 3.2 ± 1.5.

Table 2. Deuteration ratios measured towards NGC 7538-IRS1.

Species	Ratios
CH_2DOH/CH_3OH	$(3.2 \pm 0.8) \times 10^{-3}$
CH_3OD/CH_3OH	$(1.0 \pm 0.4) \times 10^{-3}$
CH_2DOH/CH_3OD	3.2 ± 1.5

4.2. Water and HDO

Water does not exhibit the same level of fractionation as methanol in low-mass star-forming regions, with a HDO/H_2O lying in the range 0.01–0.07 (Liu et al. 2011; Parise et al. 2005, 2006; Ratajczak et al. 2011; Coutens et al. 2012; Faure et al. 2015a). However, in Orion-KL water and methanol seem to be fractionated to a similar extent (Neill et al. 2013b). This is likely the result of recent desorption from ice mantles (see further details on thermal H/D exchanges between water and methanol during the warm-up phase in Faure et al. 2015a).

Although only the HDO ($2_{2,0}$–$3_{1,3}$) transition is detected in our data, as shown in Fig. 1, we can roughly estimate the D/H ratio for water combining our result with that of different studies. Indeed, combining the observed HDO integrated flux ($\sim 0.8 \pm 0.1$ K km s^{-1}) with the ones measured by Jacq et al. (1990) for the ($3_{1,2}$–$2_{2,1}$) and ($2_{1,1}$–$2_{1,2}$) transitions and assuming a source size of 3.8″, we derived a HDO column density of about 1.6×10^{15} cm^{-2} and a rotational temperature of $\sim$130 K.

From recent *Herschel*/HIFI observations of water in NGC 7538-IRS1, Herpin et al. (2017) derived a water abundance, $\chi_{(H_2O)}$, of 8×10^{-6}. Assuming a n_{H_2} of about 10^8 cm^{-3} (see Sect. 3.3), we estimate a HDO/H_2O ratio lying in the range 10^{-4}–10^{-3} according to the source size taken into account (see also van der Tak et al. 2006).

Incidentally, we note that Herpin et al. (2017) also derived a H_2O abundance of 5×10^{-5} for the very inner part of the hot core, as probed by a THz line observed with SOFIA.

These findings show that the water emission source size provides strong constraints on the deuteration ratio. Therefore, further interferometric observations of water and its isotopologs are clearly needed to investigate water fractionation in this source in more detail.

4.3. Comparison with other sources

Figure 4 reports the relative CH_2DOH/CH_3OD abundance ratio measured towards a large sample of star-forming regions, from low- to high-mass, ordered from left to right by increasing source luminosity. It is immediately apparent that there is a variation between the sources of two orders of magnitude. More specifically, in low-mass star-forming regions, methanol deuteration strongly favors the methyl group (CH_2DOH) by far more than the statistical factor (3), whereas in high-mass the opposite trend is observed.

4.4. Modeling

The value of the abundance ratio CH_2DOH/CH_3OD toward NGC 7538-IRS1 is 3.2 ± 1.5, in good agreement with the value

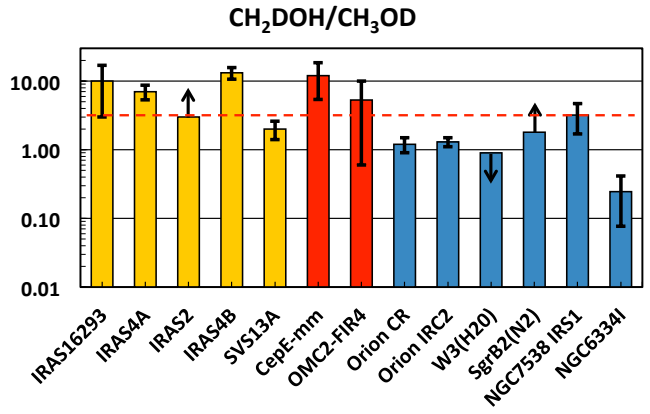

Fig. 4. CH_2DOH/CH_3OD ratios observed towards low- (yellow), intermediate- (red), and high-mass (blue) star-forming regions: IRAS 16293-2422 (Parise et al. 2002; Jørgensen et al. 2018), IRAS 4A, IRAS 2, IRAS 4B (Parise et al. 2006), SVS13A (Bianchi et al. 2017), CepE-mm (Ratajczak et al. 2011), OMC2-FIR4 (Ratajczak et al. 2011), Orion CR (Neill et al. 2013b), Orion Irc2, W3(H2O), SgrB2(N2) (Belloche et al. 2016), NGC 7538-IRS1 (this work; blue and white stripes), and NGC 6334I (Bøgelund et al. 2018). We note that values derived by Parise et al. (2006) and Ratajczak et al. (2011) were divided by a factor of 2 and 1.5, respectively, due to a spectroscopic issue (see Belloche et al. 2016). The dashed red line shows the statistical factor $CH_2DOH/CH_3OD = 3$.

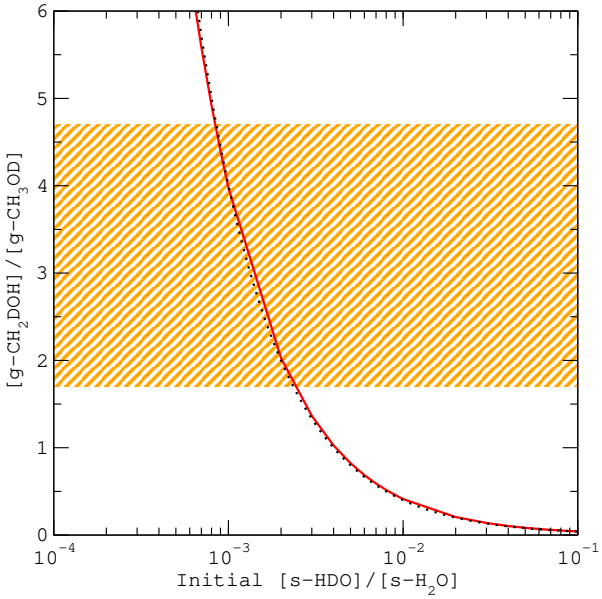

Fig. 5. Gas-phase abundance ratio of the deuterated isotopologs, CH_2DOH/CH_3OD, as function of the initial (cold) water ice deuteration. The dotted line corresponds to the analytic solution $CH_2DOH/CH_3OD = 0.004/(HDO/H_2O)$, see Faure et al. (2015a) for details.The ratio observed toward NGC 7538-IRS1 is represented by the orange hatched zone.

of three predicted by grain chemistry models (e.g., Charnley et al. 1997; Osamura et al. 2004). In these models, the deuterium fractionation of methanol proceeds in the ice during the early cold prestellar phase through the statistical addition of H and D atoms to CO molecules and the ratio s-CH_2DOH/s-CH_3OD is equal to the statistical value of three. More recent and sophisticated models also predict a ratio close to three (e.g., Bøgelund et al. 2018). These models however neglect processes occurring in the subsequent warm-up phase. In particular, Faure et al. (2015a) have shown that the s-CH_2DOH/s-CH_3OD ratio can change during this phase as a result of H/D exchanges between the hydroxyl (-OH) functional groups of methanol and water (see details in Faure et al. 2015b). This scenario was successful in explaining both the high value (>3) of the CH_2DOH/CH_3OD abundance ratio towards the low-mass protostar IRAS 16293-2422 and the low-value (<3) measured towards Orion (see Fig. 4).

We adapted the model of Faure et al. (2015a) to the conditions of NGC 7538-IRS1. First, the density was taken as $n_H = 2 \times 10^8$ cm^{-3} and the (equal) gas and dust temperatures as $T = 100$ K. The methanol abundance (by number) relative to water is 4% (Öberg et al. 2011; Boogert et al. 2015) and the mean water abundance is $5 \times 10^{-5} n_H$. The accreting D/H ratio is inferred from the observed CH_2DOH/CH_3OH ratio (see Table 2) as $\alpha_m = 1.1 \times 10^{-3}$, assuming that the initial (statistical) deuteration of CH_2DOH in the ice is conserved during the hot core phase. The post-evaporative gas-phase chemistry is also entirely neglected (full details can be found in Faure et al. 2015a). The results of the model are plotted in Fig. 5: it is found that the observed CH_2DOH/CH_3OD ratio of 3.2 ± 1.5 can be reproduced for a solid s-HDO/s-H_2O ratio in the range $\sim 8 \times 10^{-4} - 2 \times 10^{-3}$. Therefore, while the CH_2DOH/CH_3OD ratio of 3.2 ± 1.5 is consistent with a statistical deuteration, the occurrence of H/D exchanges cannot be excluded. In particular, it should be noted that H/D exchanges can explain the range of values depicted in Fig. 4, that is CH_2DOH/CH_3OD ratios in the range ~0.1−10. To our knowledge, this is currently the only mechanism able to explain the nonstatistical deuteration of methanol in both low- and high-mass protostars.

5. Conclusions

To summarize, we investigated the deuteration of methanol in the high-mass star-forming regions NGC 7538-IRS1 using IRAM-30m observations. Our study shows that the fractionation degree of deuterated methanol is low in this source. From the numerous (≥10) detected lines, we estimate a CH_2DOH/CH_3OD relative abundance ratio of 3.2 ± 1.5. Although our findings are commensurate with statistical deuteration at the icy surface of grain mantles, we cannot exclude H/D exchanges between water and methanol at the present time. Further observations of water and HDO are required to address this point.

Acknowledgements. We thank the anonymous referee for his very fruitful comments that have strengthened our paper. This work is supported by the French National Research Agency in the framework of the Investissements d'Avenir program (ANR-15-IDEX-02), through the funding of the "Origin of Life" project of the Université Grenoble-Alpes. C.F. and D.F. acknowledge support from the Italian Ministry of Education, Universities and Research, project SIR (RBSI14ZRHR). L.H.X. acknowledges financial support from the Natural Sciences and Engineering Research Council of Canada. We also acknowledge funding from the European Research Council (ERC) under the European Union's Horizon 2020 research and innovation programme, for the Project "The Dawn of Organic Chemistry" (DOC), grant agreement No 741002. This project was carried out under project number 128–12 with the IRAM 30 m telescope. IRAM is supported by INSU/CNRS (France), MPG (Germany), and IGN (Spain).

References

Belloche, A., Müller, H. S. P., Garrod, R. T., & Menten, K. M. 2016, A&A, 587, A91
Beuther, H., Linz, H., & Henning, T. 2012, A&A, 543, A88
Bianchi, E., Codella, C., Ceccarelli, C., et al. 2017, MNRAS, 467, 3011
Bisschop, S. E., Jørgensen, J. K., van Dishoeck, E. F., & de Wachter, E. B. M. 2007, A&A, 465, 913

Bøgelund, E. G., McGuire, B. A., Ligterink, N. F. W., et al. 2018, A&A, 615, A88
Boogert, A. C. A., Gerakines, P. A., & Whittet, D. C. B. 2015, ARA&A, 53, 541
Caselli, P., & Ceccarelli, C. 2012, A&ARv, 20, 56
Ceccarelli, C., Caselli, P., Herbst, E., Tielens, A. G. G. M., & Caux, E. 2007, Protostars and Planets V (Tucson: University of Arizona Press), 47
Ceccarelli, C., Caselli, P., Bockelée-Morvan, D., et al. 2014, Protostars and Planets VI (Tucson: University of Arizona Press), 859
Charnley, S. B., Tielens, A. G. G. M., & Rodgers, S. D. 1997, ApJ, 482, L203
Coutens, A., Vastel, C., Caux, E., et al. 2012, A&A, 539, A132
Faure, A., Faure, M., Theulé, P., Quirico, E., & Schmitt, B. 2015a, A&A, 584, A98
Faure, M., Quirico, E., Faure, A., et al. 2015b, Icarus, 261, 14
Goldsmith, P. F., & Langer, W. D. 1999, ApJ, 517, 209
Herpin, F., Baudry, A., Richards, A. M. S., et al. 2017, A&A, 606, A52
Jacq, T., Walmsley, C. M., Henkel, C., et al. 1990, A&A, 228, 447
Jacq, T., Walmsley, C. M., Mauersberger, R., et al. 1993, A&A, 271, 276
Jørgensen, J. K., Müller, H. S. P., Calcutt, H., et al. 2018, A&A, 620, A17
Lis, D. C., Roueff, E., Gerin, M., et al. 2002, ApJ, 571, L55
Liu, F.-C., Parise, B., Kristensen, L., et al. 2011, A&A, 527, A19
Müller, H. S. P., Menten, K. M., & Mäder, H. 2004, A&A, 428, 1019
Müller, H. S. P., Schlöder, F., Stutzki, J., & Winnewisser, G. 2005, J. Mol. Struct., 742, 215
Nandi, A., Qu, C., & Bowman, J. M. 2019, J. Comput. Chem., 40, 328
Neill, J. L., Crockett, N. R., Bergin, E. A., Pearson, J. C., & Xu, L.-H. 2013a, ApJ, 777, 85
Neill, J. L., Wang, S., Bergin, E. A., et al. 2013b, ApJ, 770, 142
Öberg, K. I., Boogert, A. C. A., Pontoppidan, K. M., et al. 2011, ApJ, 740, 109
Osamura, Y., Roberts, H., & Herbst, E. 2004, A&A, 421, 1101
Parise, B., Ceccarelli, C., Tielens, A. G. G. M., et al. 2002, A&A, 393, L49
Parise, B., Castets, A., Herbst, E., et al. 2004, A&A, 416, 159
Parise, B., Caux, E., Castets, A., et al. 2005, A&A, 431, 547
Parise, B., Ceccarelli, C., Tielens, A. G. G. M., et al. 2006, A&A, 453, 949
Pearson, J. C., Yu, S., & Drouin, B. J. 2012, J. Mol. Spectr., 280, 119
Peng, T.-C., Despois, D., Brouillet, N., Parise, B., & Baudry, A. 2012, A&A, 543, A152
Pickett, H. M., Poynter, I. R. L., Cohen, E. A., et al. 1998, J. Quant. Spectr. Rad. Transf., 60, 883
Rabli, D., & Flower, D. R. 2010, MNRAS, 406, 95
Ratajczak, A., Taquet, V., Kahane, C., et al. 2011, A&A, 528, L13
Roberts, H., Fuller, G. A., Millar, T. J., Hatchell, J., & Buckle, J. V. 2002, Planet. Space Sci., 50, 1173
van der Tak, F. F. S., Walmsley, C. M., Herpin, F., & Ceccarelli, C. 2006, A&A, 447, 1011
van der Tak, F. F. S., Black, J. H., Schöier, F. L., Jansen, D. J., & van Dishoeck, E. F. 2007, A&A, 468, 627
Walsh, M. S., Xu, L.-H., Lees, R. M., et al. 2000, J. Mol. Spectr., 204, 60
Wilson, T. L. 1999, Rep. Prog. Phys., 62, 143
Wirström, E. S., Geppert, W. D., Hjalmarson, Å., et al. 2011, A&A, 533, A24
Xu, L. H., & Hougen, J. T. 1995a, J. Mol. Spectr., 169, 396
Xu, L. H., & Hougen, J. T. 1995b, J. Mol. Spectr., 173, 540
Xu, L.-H., & Lovas, F. J. 1997, J. Phys. Chem. Ref. Data, 26, 17
Xu, L.-H., Walsh, M. S., & Lees, R. M. 1996, J. Mol. Spectr., 179, 269
Xu, L.-H., Fisher, J., Lees, R. M., et al. 2008, J. Mol. Spectr., 251, 305
Xu, L.-H., Lees, R. M., Hao, Y., et al. 2014, J. Mol. Spectr., 303, 1

Appendix A: Spectroscopic and observational line parameters

Tables A.1–A.4 list the spectroscopic and observational line parameters for the observed CH_3OH-A, CH_3OH-E, $^{13}CH_3OH$, CH_2DOH, CH_3OD-A and CH_3OD-E transitions.

Table A.1. Methanol.

Species	Frequency (MHz)	Quantum numbers	E_{up} (K)	A_{ul} (10^{-5} s^{-1})	Flux (K km s^{-1})	V_{lsr} (km s^{-1})	ΔV (km s^{-1})	T_{peak} (mK)
CH_3OH-E	213 159.150	$20_{-4,0} - 19_{-5,0}$	567.0	1.6	1.6 (0.3)	−59.0 (0.0)	4.0 (0.1)	374 (9)
	213 377.528	$13_{6,0} - 14_{5,0}$	382.0	1.1	1.4 (0.3)	−59.0 (0.0)	3.5 (0.1)	368 (7)
	213 427.061	$1_{1,0} - 0_{0,0}$	15.5	3.4	4.4 (0.9)	−58.8 (0.0)	3.5 (0.0)	1173 (18)
	217 886.504	$20_{1,0} - 20_{0,0}$	500.5	3.4	1.8 (0.4)	−59.2 (0.0)	3.7 (0.0)	439 (5)
	218 440.063	$4_{2,0} - 3_{1,0}$	37.6	4.7	10.0 (2.0)	−58.1 (0.0)	5.3 (0.1)	1776 (12)
	219 983.675	$25_{3,0} - 24_{4,0}$	794.3	2.0	0.4 (0.1)	−59.0 (0.1)	3.1 (0.3)	130 (13)
	219 993.658	$23_{5,0} - 22_{6,0}$	768.0	1.7	0.6 (0.1)	−58.9 (0.1)	3.8 (0.2)	143 (8)
	220 078.561	$8_{0,0} - 7_{1,0}$	88.7	2.5	2.9 (0.6)	−58.7 (0.0)	4.1 (0.1)	677 (7)
	229 589.056	$15_{4,0} - 16_{3,0}$	366.5	2.1	2.2 (0.4)	−59.1 (0.0)	3.1 (0.1)	651 (14)
	229 758.756	$8_{-1,0} - 7_{0,0}$	81.2	4.2	5.0 (1.0)	−58.3 (0.0)	4.2 (0.0)	1124 (11)
	230 027.047	$3_{-2,0} - 4_{-1,0}$	31.9	1.5	3.0 (0.6)	−58.6 (0.0)	4.2 (0.1)	658 (14)
	230 368.763	$22_{4,0} - 21_{5,0}$	674.8	2.1	1.1 (0.2)	−59.0 (0.2)	3.9 (0.5)	274 (62)
	232 624.811	$15_{6,1} - 15_{7,1}$	861.9	0.7	0.3 (0.1)	−58.8 (0.1)	3.3 (0.3)	74 (6)
	232 645.103	$8_{6,1} - 8_{7,1}$	667.7	0.9	0.4 (0.1)	−58.8 (0.2)	4.1 (0.4)	84 (7)
	232 847.103	$9_{6,1} - 9_{7,1}$	688.6	1.0	0.5 (0.1)	−59.0 (0.1)	4.2 (0.3)	106 (6)
	232 945.797	$10_{-3,0} - 11_{-2,0}$	182.5	2.1	3.8 (0.8)	−59.0 (0.0)	3.6 (0.1)	999 (15)
	233 011.878	$10_{6,1} - 10_{7,1}$	711.7	1.1	0.3 (0.1)	−58.7 (0.2)	3.3 (0.4)	87 (9)
	233 121.162	$11_{6,1} - 11_{7,1}$	737.1	1.1	0.5 (0.1)	−59.2 (0.2)	4.2 (0.5)	113 (10)
	233 155.874	$12_{6,1} - 12_{7,1}$	764.9	1.0	0.3 (0.1)	−59.0 (0.3)	4.0 (0.8)	68 (10)
	234 698.519	$5_{-4,0} - 6_{-3,0}$	114.8	0.6	1.8 (0.4)	−59.0 (0.0)	3.3 (0.0)	527 (6)
	244 337.983	$9_{1,1} - 8_{0,1}$	387.7	4.0	1.5 (0.3)	−59.4 (0.1)	4.4 (0.1)	329 (9)
	245 094.503	$18_{-6,1} - 17_{-7,1}$	881.0	2.1	0.2 (0.0)	−58.6 (0.2)	3.0 (0.4)	67 (7)
	247 161.950	$16_{2,0} - 15_{3,0}$	330.2	2.6	1.9 (0.4)	−59.3 (0.0)	3.5 (0.1)	518 (12)
	247 840.050	$12_{-2,1} - 13_{-3,1}$	537.2	6.3	1.7 (0.3)	−58.9 (0.0)	3.7 (0.1)	434 (8)
	247 968.119	$23_{1,0} - 23_{0,0}$	653.5	4.4	1.0 (0.2)	−59.0 (0.0)	4.1 (0.1)	228 (5)
	248 854.996	$15_{-1,1} - 16_{-2,1}$	683.3	1.3	0.4 (0.1)	−58.7 (0.1)	3.6 (0.2)	107 (5)
	249 004.019	$10_{7,1} - 9_{6,1}$	700.5	3.6	0.5 (0.1)	−58.7 (0.1)	3.9 (0.2)	114 (6)
	249 192.836	$16_{-3,0} - 15_{-4,0}$	370.4	2.5	1.6 (0.3)	−59.0 (0.0)	4.0 (0.1)	376 (6)
	250 970.042	$17_{3,1} - 18_{4,1}$	763.1	7.7	1.0 (0.2)	−59.0 (0.1)	3.7 (0.1)	250 (7)
	254 015.377	$2_{0,0} - 1_{-1,0}$	12.2	1.9	3.1 (0.6)	−58.9 (0.3)	4.1 (0.3)	704 (104)
	254 419.419	$11_{5,0} - 12_{4,0}$	281.3	1.8	1.8 (0.4)	−58.7 (0.0)	3.2 (0.1)	536 (9)
	259 581.398	$24_{1,0} - 24_{0,0}$	709.1	4.9	0.7 (0.1)	−59.0 (0.1)	3.4 (0.2)	191 (8)
	261 061.320	$21_{-4,0} - 20_{-5,0}$	615.7	3.0	1.0 (0.2)	−58.8 (0.1)	2.9 (0.3)	327 (29)
	261 704.409	$12_{6,0} - 13_{5,0}$	351.9	1.8	1.1 (0.2)	−59.2 (0.1)	3.4 (0.2)	301 (19)
	261 805.675	$2_{1,0} - 1_{0,0}$	20.1	5.6	5.3 (1.1)	−58.2 (0.0)	4.4 (0.1)	1132 (15)
	264 732.426	$13_{2,1} - 12_{3,1}$	602.6	0.5	0.2 (0.1)	−58.6 (0.2)	3.0 (0.4)	75 (10)
	265 289.562	$6_{1,0} - 5_{2,0}$	61.9	2.6	1.5 (0.3)	−59.0 (0.0)	2.9 (0.2)	497 (40)
	266 838.148	$5_{2,0} - 4_{1,0}$	49.2	7.7	3.9 (0.8)	−57.9 (0.0)	3.5 (0.1)	1052 (24)
	267 887.317	$24_{5,0} - 23_{6,0}$	823.6	3.2	0.5 (0.1)	−59.1 (0.2)	3.5 (0.4)	127 (13)
	268 743.954	$9_{-5,0} - 10_{-4,0}$	220.5	1.8	1.8 (0.4)	−59.2 (0.1)	3.8 (0.2)	449 (23)
	271 222.675	$26_{3,0} - 25_{4,0}$	854.6	3.8	0.7 (0.1)	−58.7 (0.2)	4.3 (0.4)	154 (11)
	271 933.603	$25_{1,0} - 25_{0,0}$	767.0	5.5	0.9 (0.2)	−59.0 (0.1)	3.6 (0.3)	230 (18)
	274 022.001	$24_{-7,0} - 25_{-6,0}$	947.6	3.1	0.2 (0.1)	−58.9 (0.2)	3.8 (0.5)	60 (6)

Table A.2. Methanol.

Species	Frequency (MHz)	Quantum numbers	E_{up} (K)	A_{ul} (10^{-5} s^{-1})	Flux (K km s^{-1})	V_{lsr} (km s^{-1})	ΔV (km s^{-1})	T_{peak} (mK)
CH_3OH-A	215 302.206	$6_{1,+,1} - 7_{2,+,1}$	373.8	4.2	2.4 (0.5)	−59.1 (0.0)	3.6 (0.1)	637 (8)
	217 299.205	$6_{1,-,1} - 7_{2,-,1}$	373.9	4.3	1.8 (0.4)	−59.0 (0.0)	3.1 (0.1)	530 (23)
	231 281.110	$10_{2,-,0} - 9_{3,-,0}$	165.3	1.8	1.7 (0.3)	−59.0 (0.0)	3.5 (0.1)	460 (18)
	232 418.521	$10_{2,+,0} - 9_{3,+,0}$	165.4	1.9	1.6 (0.3)	−58.9 (0.0)	3.0 (0.1)	518 (16)
	232 783.446	$18_{3,+,0} - 17_{4,+,0}$	446.5	2.2	2.4 (0.5)	−59.2 (0.0)	3.8 (0.1)	589 (7)
	233 795.666	$18_{3,-,0} - 17_{4,-,0}$	446.6	2.2	2.4 (0.5)	−59.2 (0.0)	3.6 (0.0)	617 (7)
	234 683.370	$4_{2,-,0} - 5_{1,-,0}$	60.9	1.8	3.7 (0.7)	−58.9 (0.0)	3.6 (0.0)	955 (9)
	243 915.788	$5_{1,-,0} - 4_{1,-,0}$	49.7	6.0	6.1 (1.2)	−58.0 (0.0)	4.2 (0.0)	1345 (9)
	246 873.301	$19_{3,-,0} - 19_{2,+,0}$	490.7	8.0	1.5 (0.3)	−59.2 (0.0)	3.3 (0.1)	442 (9)
	247 228.587	$4_{2,+,0} - 5_{1,+,0}$	60.9	2.2	3.5 (0.7)	−59.0 (0.0)	3.7 (0.1)	876 (14)
	247 610.918	$18_{3,-,0} - 18_{2,+,0}$	446.6	8.1	1.5 (0.3)	−59.2 (0.0)	3.3 (0.1)	437 (9)
	248 282.424	$17_{3,-,0} - 17_{2,+,0}$	404.8	8.1	1.7 (0.3)	−59.2 (0.0)	3.6 (0.1)	444 (6)
	248 885.468	$16_{3,-,0} - 16_{2,+,0}$	365.4	8.2	1.8 (0.4)	−59.2 (0.0)	3.4 (0.1)	482 (9)
	249 419.924	$15_{3,-,0} - 15_{2,+,0}$	328.3	8.2	1.8 (0.4)	−59.2 (0.0)	3.5 (0.1)	479 (11)
	249 443.301	$7_{4,-,0} - 8_{3,-,0}$	145.3	1.5	1.6 (0.3)	−59.1 (0.0)	4.0 (0.1)	375 (8)
	249 451.842	$7_{4,+,0} - 8_{3,+,0}$	145.3	1.5	1.5 (0.3)	−59.1 (0.0)	3.9 (0.1)	372 (8)
	249 887.467	$14_{3,-,0} - 14_{2,+,0}$	293.5	8.2	1.5 (0.3)	−59.2 (0.0)	3.1 (0.1)	443 (14)
	250 291.181	$13_{3,-,0} - 13_{2,+,0}$	261.0	8.2	2.0 (0.4)	−59.1 (0.0)	3.6 (0.1)	526 (8)
	250 506.853	$11_{0,+,0} - 10_{1,+,0}$	153.1	4.2	2.6 (0.5)	−58.6 (0.0)	4.5 (0.1)	535 (7)
	250 635.200	$12_{3,-,0} - 12_{2,+,0}$	230.8	8.2	2.3 (0.5)	−59.3 (0.0)	3.7 (0.1)	590 (8)
	250 924.398	$11_{3,-,0} - 11_{2,+,0}$	203.0	8.2	2.5 (0.5)	−59.2 (0.0)	3.5 (0.0)	673 (5)
	251 164.108	$10_{3,-,0} - 10_{2,+,0}$	177.5	8.2	2.7 (0.5)	−59.1 (0.0)	3.5 (0.1)	711 (12)
	251 517.309	$8_{3,-,0} - 8_{2,+,0}$	133.4	7.9	3.1 (0.6)	−59.0 (0.0)	3.5 (0.1)	835 (10)
	251 641.787	$7_{3,-,0} - 7_{2,+,0}$	114.8	7.7	3.2 (0.6)	−59.0 (0.0)	3.8 (0.1)	797 (9)
	251 738.437	$6_{3,-,0} - 6_{2,+,0}$	98.5	7.4	3.4 (0.7)	−58.8 (0.0)	4.0 (0.0)	800 (8)
	251 811.956	$5_{3,-,0} - 5_{2,+,0}$	84.6	7.0	3.6 (0.7)	−58.8 (0.0)	4.3 (0.1)	790 (17)
	251 866.524	$4_{3,-,0} - 4_{2,+,0}$	73.0	6.1	3.1 (0.6)	−58.6 (0.0)	4.1 (0.1)	717 (8)
	251 890.886	$5_{3,+,0} - 5_{2,-,0}$	84.6	7.0	3.3 (0.7)	−58.5 (0.0)	3.8 (0.1)	818 (8)
	251 895.728	$6_{3,+,0} - 6_{2,-,0}$	98.5	7.5	3.4 (0.7)	−58.6 (0.0)	3.8 (0.1)	817 (7)
	251 900.452	$4_{3,+,0} - 4_{2,-,0}$	73.0	6.1	3.4 (0.7)	−58.5 (0.0)	4.0 (0.1)	781 (9)
	251 905.729	$3_{3,-,0} - 3_{2,+,0}$	63.7	4.4	3.4 (0.7)	−58.7 (0.0)	4.2 (0.1)	629 (8)
	251 917.065	$3_{3,+,0} - 3_{2,-,0}$	63.7	4.4	3.0 (0.6)	−58.8 (0.0)	4.1 (0.1)	683 (9)
	251 923.701	$7_{3,+,0} - 7_{2,-,0}$	114.8	7.8	3.2 (0.7)	−58.8 (0.0)	3.8 (0.0)	793 (6)
	251 984.837	$8_{3,+,0} - 8_{2,-,0}$	133.4	8.0	3.1 (0.6)	−59.0 (0.0)	3.7 (0.1)	780 (10)
	252 090.409	$9_{3,+,0} - 9_{2,-,0}$	154.2	8.1	3.2 (0.6)	−59.0 (0.0)	3.7 (0.1)	799 (9)
	252 252.849	$10_{3,+,0} - 10_{2,-,0}$	177.5	8.3	2.9 (0.6)	−59.1 (0.0)	3.6 (0.0)	749 (8)
	252 485.675	$11_{3,+,0} - 11_{2,-,0}$	203.0	8.4	2.7 (0.5)	−59.1 (0.0)	3.6 (0.0)	708 (8)
	252 803.388	$12_{3,+,0} - 12_{2,-,0}$	230.8	8.4	2.5 (0.5)	−59.2 (0.0)	3.5 (0.1)	677 (9)
	253 221.376	$13_{3,+,0} - 13_{2,-,0}$	261.0	8.5	2.4 (0.5)	−59.2 (0.0)	3.4 (0.1)	660 (9)
	253 755.809	$14_{3,+,0} - 14_{2,-,0}$	293.5	8.6	2.5 (0.5)	−59.2 (0.0)	3.4 (0.1)	694 (11)
	254 423.520	$15_{3,+,0} - 15_{2,-,0}$	328.3	8.7	2.6 (0.5)	−59.2 (0.0)	3.7 (0.1)	674 (10)
	255 241.888	$16_{3,+,0} - 16_{2,-,0}$	365.4	8.8	2.2 (0.4)	−59.2 (0.0)	3.3 (0.1)	615 (8)
	256 228.714	$17_{3,+,0} - 17_{2,-,0}$	404.8	9.0	1.9 (0.4)	−59.3 (0.0)	3.3 (0.1)	545 (10)
	257 402.086	$18_{3,+,0} - 18_{2,-,0}$	446.5	9.1	2.8 (0.6)	−59.9 (0.0)	4.3 (0.1)	613 (14)
	258 780.248	$19_{3,+,0} - 19_{2,-,0}$	490.6	9.3	2.1 (0.4)	−59.4 (0.0)	3.9 (0.1)	502 (11)
	263 793.875	$5_{1,+,1} - 6_{2,+,1}$	360.0	8.2	2.7 (0.5)	−58.5 (0.1)	4.5 (0.1)	566 (13)
	265 224.426	$5_{1,-,1} - 6_{2,-,1}$	360.0	8.3	2.2 (0.4)	−59.0 (0.0)	3.6 (0.1)	569 (9)
	267 406.071	$17_{1,+,0} - 16_{2,+,0}$	366.3	4.2	5.3 (1.1)	−56.9 (0.1)	7.3 (0.2)	681 (9)
	260 381.463	$20_{3,+,0} - 20_{2,-,0}$	536.9	9.4	2.3 (0.5)	−59.8 (0.1)	4.8 (0.1)	438 (11)
	246 074.605	$20_{3,-,0} - 20_{2,+,0}$	537.0	8.0	1.7 (0.3)	−59.5 (0.0)	3.7 (0.1)	417 (10)
	229 939.095	$19_{5,-,0} - 20_{4,-,0}$	578.6	2.1	1.3 (0.3)	−59.0 (0.1)	3.9 (0.2)	315 (12)
	229 864.121	$19_{5,+,0} - 20_{4,+,0}$	578.6	2.1	1.4 (0.3)	−58.8 (0.1)	4.8 (0.2)	281 (9)
	262 223.872	$21_{3,+,0} - 21_{2,-,0}$	585.6	9.7	1.3 (0.3)	−59.3 (0.0)	3.5 (0.1)	350 (10)
	245 223.019	$21_{3,-,0} - 21_{2,+,0}$	585.7	7.9	1.9 (0.4)	−58.6 (0.2)	4.3 (0.2)	408 (13)
	264 325.354	$22_{3,+,0} - 22_{2,-,0}$	636.6	9.9	1.5 (0.3)	−59.3 (0.1)	4.3 (0.2)	325 (14)
	244 330.372	$22_{3,-,0} - 22_{2,+,0}$	636.8	7.8	1.5 (0.3)	−59.3 (0.0)	3.9 (0.1)	362 (8)
	271 562.485	$17_{2,+,1} - 16_{1,+,1}$	652.6	6.5	1.4 (0.3)	−59.2 (0.1)	4.4 (0.2)	307 (12)
	259 273.686	$17_{2,-,1} - 16_{1,-,1}$	652.7	5.6	1.1 (0.2)	−59.0 (0.0)	3.8 (0.1)	270 (6)
	266 703.383	$23_{3,+,0} - 23_{2,-,0}$	689.9	10.2	1.0 (0.2)	−59.3 (0.0)	3.2 (0.1)	306 (7)
	266 872.190	$14_{6,+,1} - 15_{5,+,1}$	711.0	3.1	0.9 (0.2)	−59.0 (0.1)	3.6 (0.2)	234 (10)
	269 374.884	$24_{3,+,0} - 24_{2,-,0}$	745.5	10.5	1.2 (0.3)	−59.2 (0.1)	3.7 (0.3)	310 (21)
	217 642.677	$15_{6,-,1} - 16_{5,-,1}$	745.6	1.9	1.1 (0.2)	−58.8 (0.1)	4.4 (0.1)	234 (7)
	272 356.098	$25_{3,+,0} - 25_{2,-,0}$	803.4	10.9	1.2 (0.2)	−59.2 (0.0)	3.6 (0.2)	308 (8)
	233 916.950	$13_{3,-,2} - 14_{4,-,2}$	868.5	1.4	0.4 (0.1)	−58.7 (0.1)	3.6 (0.2)	115 (4)
	233 917.018	$13_{3,+,2} - 14_{4,+,2}$	868.5	1.4	0.4 (0.1)	−58.7 (0.1)	3.5 (0.3)	111 (7)
	268 345.816	$20_{4,-,1} - 21_{5,-,1}$	967.6	5.3	0.8 (0.2)	−58.9 (0.1)	4.1 (0.3)	189 (14)
	268 346.226	$20_{4,+,1} - 21_{5,+,1}$	967.6	5.3	0.8 (0.2)	−58.5 (0.2)	4.1 (0.4)	189 (14)

Table A.3. ^{13}C methanol.

Species	Frequency (MHz)	Quantum numbers	E_{up} (K)	A_{ul} (10^{-5} s^{-1})	Flux (K km s^{-1})	V_{lsr} (km s^{-1})	ΔV (km s^{-1})	T_{peak} (mK)
$^{13}CH_3OH$	212 775.66	$1_{1,0,0} - 0_{0,0,0}$	23.3	3.3	296 (60)	−58.8 (0.1)	2.7 (0.2)	104 (8)
	215 707.92	$8_{4,5,-,0} - 9_{3,6,-,0}$	162.3	1.1	134 (33)	−58.7 (0.3)	2.5 (0.7)	51 (12)
	215 722.48	$8_{4,4,+,0} - 9_{3,7,+,0}$	162.3	1.1	222 (45)	−58.9 (0.1)	3.3 (0.2)	63 (2)
	216 370.39	$10_{2,9,-,0} - 9_{3,6,-,0}$	162.4	1.5	540 (113)	−59.5 (0.2)	4.9 (0.5)	103 (8)
	234 011.58	$5_{1,5,+,0} - 4_{1,4,+,0}$	48.3	5.3	1093 (220)	−58.8 (0.0)	3.5 (0.2)	290 (12)
	235 881.17	$5_{0,5,0} - 4_{0,4,0}$	47.1	5.6	1044 (209)	−58.8 (0.0)	3.2 (0.1)	307 (7)
	235 938.22	$5_{-1,5,0} - 4_{-1,4,0}$	39.6	5.4	1092 (221)	−58.8 (0.1)	3.2 (0.2)	318 (18)
	235 960.37	$5_{0,5,+,0} - 4_{0,4,+,0}$	34.0	5.6	1032 (207)	−58.7 (0.0)	3.1 (0.0)	316 (4)
	235 971.07	$5_{4,2,-,0} - 4_{4,1,-,0}$	114.8	2.0	498 (103)	−58.6 (0.1)	2.7 (0.3)	176 (19)
	235 971.07	$5_{4,1,+,0} - 4_{4,0,+,0}$	114.8	2.0	502 (101)	−58.6 (0.0)	2.7 (0.1)	175 (6)
	235 978.62	$5_{-4,2,0} - 4_{-4,1,0}$	122.3	2.0	307 (64)	−58.9 (0.2)	2.6 (0.6)	110 (19)
	235 997.23	$5_{3,3,+,0} - 4_{3,2,+,0}$	84.0	3.6	1772 (360)	−57.9 (0.1)	4.6 (0.3)	360 (17)
	235 997.23	$5_{3,2,-,0} - 4_{3,1,-,0}$	84.0	3.6	1771 (360)	−57.9 (0.1)	4.6 (0.3)	360 (18)
	236 008.39	$5_{2,4,-,0} - 4_{2,3,-,0}$	71.8	4.8	1390 (287)	−57.6 (0.2)	5.1 (0.5)	258 (19)
	236 006.10	$5_{3,2,0} - 4_{3,1,0}$	81.9	3.6	1459 (299)	-60.6 (0.2)	5.4 (0.5)	253 (15)
	236 016.55	$5_{-3,3,0} - 4_{-3,2,0}$	96.9	3.6	428 (90)	−58.7 (0.1)	2.5 (0.4)	162 (20)
	236 041.40	$5_{1,4,0} - 4_{1,3,0}$	55.0	5.5	1002 (202)	−58.7 (0.0)	3.5 (0.1)	267 (8)
	236 049.52	$5_{2,3,+,0} - 4_{2,2,+,0}$	71.8	4.8	1300 (260)	−58.5 (0.0)	3.7 (0.1)	332 (5)
	236 062.00	$5_{-2,4,0} - 4_{-2,3,0}$	60.0	4.7	1971 (397)	−59.3 (0.1)	4.3 (0.1)	432 (13)
	236 062.85	$5_{2,3,0} - 4_{2,2,0}$	56.3	4.7	1973 (397)	−58.2 (0.1)	4.3 (0.2)	431 (18)
	248 654.97	$10_{-3,8,0} - 11_{-2,10,0}$	187.5	2.6	234 (48)	−58.4 (0.1)	2.4 (0.2)	91 (7)
	250 125.69	$5_{3,2,0} - 6_{2,4,0}$	81.9	1.6	164 (34)	−58.5 (0.1)	2.8 (0.3)	54 (5)
	250 784.61	$2_{0,2,0} - 1_{-1,1,0}$	19.9	1.8	179 (37)	−58.7 (0.1)	2.8 (0.3)	61 (6)
	254 321.72	$4_{2,2,+,0} - 5_{1,5,+,0}$	60.5	2.3	365 (74)	−58.6 (0.1)	3.1 (0.2)	112 (6)
	254 509.36	$10_{3,7,-,0} - 10_{2,8,+,0}$	174.6	8.5	1190 (239)	−58.7 (0.0)	3.3 (0.1)	340 (10)
	254 959.40	$7_{3,4,-,0} - 7_{2,5,+,0}$	113.5	8.1	1042 (209)	−58.8 (0.0)	3.1 (0.1)	314 (9)
	255 050.97	$6_{3,3,-,0} - 6_{2,4,+,0}$	97.6	7.8	1569 (315)	−58.6 (0.1)	3.9 (0.1)	383 (12)
	251 796.08	$17_{3,14,-,0} - 17_{2,15,+,0}$	396.5	8.6	465 (94)	−58.6 (0.1)	3.3 (0.1)	131 (5)
	259 036.49	$17_{3,15,+,0} - 17_{2,16,-,0}$	396.5	9.1	667 (135)	−57.8 (0.1)	4.1 (0.2)	152 (6)
	252 870.23	$15_{3,12,-,0} - 15_{2,13,+,0}$	321.8	8.7	697 (140)	−58.7 (0.0)	3.4 (0.1)	191 (3)
	257 421.79	$15_{3,13,+,0} - 15_{2,14,-,0}$	321.8	9.0	607 (122)	−58.5 (0.0)	3.3 (0.1)	175 (5)
	256 826.57	$14_{3,12,+,0} - 14_{2,13,-,0}$	287.8	8.9	758 (153)	−58.7 (0.1)	3.2 (0.2)	221 (9)
	273 962.69	$11_{5,7,0} - 12_{4,8,0}$	286.2	2.2	103 (24)	−58.7 (0.2)	1.8 (0.5)	52 (14)
	269 530.49	$15_{-1,15,0} - 14_{-2,13,0}$	277.0	3.1	324 (81)	−58.0 (0.3)	2.8 (0.8)	107 (25)

Table A.4. Deuterated methanol.

Species	Frequency (MHz)	Quantum numbers	E_{up} (K)	A_{ul} (10^{-5} s^{-1})	Flux (K km s^{-1})	V_{lsr} (km s^{-1})	ΔV (km s^{-1})	T_{peak} (mK)
CH_2DOH	234 471.03	$8_{2,6,0} - 8_{1,7,0}$	93.7	8.4	171 (38)	−57.5 (0.2)	2.8 (0.4)	57 (6)
	255 647.82	$3_{2,2,0} - 3_{1,3,0}$	29.0	6.3	101 (28)	−57.9 (0.3)	2.3 (0.8)	41 (11)
	256 731.55	$4_{1,4,0} - 3_{0,3,0}$	25.2	6.9	126 (31)	−58.2 (0.3)	3.4 (0.7)	35 (6)
	258 337.11	$4_{2,3,0} - 4_{1,4,0}$	37.6	7.0	101 (29)	−58.8 (0.3)	2.9 (0.7)	33 (7)
	264 017.72	$6_{1,6,0} - 5_{1,5,0}$	48.4	5.8	182 (51)	−58.2 (0.3)	2.5 (0.6)	68 (14)
	265 509.20	$6_{1,6,2} - 5_{1,5,2}$	67.5	7.5	126 (30)	−58.0 (0.2)	2.5 (0.5)	48 (7)
	265 682.51	$6_{2,5,0} - 6_{1,6,0}$	61.2	8.2	126 (32)	−58.1 (0.2)	3.0 (0.6)	40 (7)
	267 634.61	$6_{0,6,0} - 5_{0,5,0}$	45.0	6.3	187 (40)	−58.2 (0.1)	2.3 (0.2)	77 (6)
	267 731.74	$6_{2,5,1} - 5_{2,4,1}$	71.6	7.1	163 (38)	−57.9 (0.1)	2.4 (0.4)	64 (8)
	267 741.09	$6_{3,4,1} - 5_{3,3,1}$	89.9	5.9	258 (54)	−58.6 (0.1)	3.2 (0.3)	76 (5)
	267 742.05	$6_{3,3,1} - 5_{3,2,1}$	89.9	5.9	261 (55)	−57.5 (0.1)	3.3 (0.3)	76 (5)
	270 299.93	$7_{2,6,0} - 7_{1,70}$	76.2	8.8	117(31)	−57.8 (0.1)	2.6 (0.3)	43 (4)
	270 734.57	$6_{1,5,1} - 5_{1,4,1}$	62.0	7.8	187 (41)	−58.3 (0.1)	2.5 (0.3)	69 (7)
CH_3OD-E	217 132.73	$9_{1,8,0} - 8_{2,6,0}$	107.32	1.7	115 (28)	−58.0 (0.3)	4.2 (0.9)	26 (5)
	245 143.16	$5_{-1,5,0} - 4_{0,4,0}$	37.27	5.9	212 (54)	−58.6 (0.3)	3.8 (0.7)	53 (12)
	252 624.31	$6_{0,6,0} - 5_{-1,5,0}$	49.39	5.0	207 (47)	−57.6 (0.1)	2.8 (0.3)	70 (10)
	264 576.81	$10_{1,9,0} - 9_{2,7,0}$	129.23	3.0	115 (31)	−59.0 (0.3)	3.4 (1.0)	31 (8)
	269 844.66	$4_{-2,3,0} - 4_{-1,4,0}$	39.36	11.1	156 (46)	−58.9 (0.3)	1.9 (0.4)	75 (18)
	270 581.30	$5_{-2,4,0} - 5_{-1,5,0}$	50.25	11.6	310 (65)	−58.6 (0.1)	3.2 (0.3)	90 (8)
	271 079.19	$6_{-1,6,0} - 5_{-1,5,0}$	50.27	7.5	416 (88)	−58.4 (0.1)	3.6 (0.3)	109 (12)
	271 417.31	$6_{0,6,0} - 5_{0,5,0}$	49.39	6.1	332 (73)	−57.9 (0.3)	3.9 (0.8)	80 (12)
	272 328.66	$6_{2,4,0} - 5_{2,3,0}$	64.21	6.9	187 (48)	−58.3 (0.2)	3.0 (0.5)	58 (13)
	272 922.56	$6_{1,5,0} - 5_{1,4,0}$	54.83	7.7	435 (101)	−57.5 (0.3)	3.8 (0.6)	108 (20)
CH_3OD-A	218 156.16	$14_{1,13,0} - 14_{0,14,0}$	237.96	9.1	259 (54)	−57.5 (0.4)	3.1 (0.7)	79 (6)
	230 105.09	$5_{1,4,0} - 4_{1,3,0}$	39.53	4.4	286 (77)	−58.2 (0.3)	2.8 (0.6)	94 (21)
	232 077.53	$15_{1,14,0} - 15_{0,15,0}$	270.96	10.5	740 (150)	−56.9 (0.2)	3.9 (0.4)	180 (8)
	246 522.69	$8_{0,8,0} - 7_{1,7,0}$	78.24	8.6	596 (127)	−58.9 (0.7)	6.3 (2.2)	89 (13)
	265 235.75	$3_{1,3,0} - 2_{0,2,0}$	19.26	13.2	310 (66)	−58.4 (0.1)	3.1 (0.3)	94 (10)
	271 704.94	$6_{0,6,0} - 5_{0,5,0}$	45.67	7.6	244 (72)	−58.8 (0.2)	2.8 (0.4)	81 (24)
	271 843.69	$14_{2,12,0} - 14_{1,13,0}$	251	16.5	247 (62)	−58.5 (0.4)	3.4 (0.8)	69 (15)
	272 004.50	$6_{2,5,0} - 5_{2,4,0}$	67.49	6.9	295 (67)	−58.1 (0.3)	3.3 (0.7)	83 (13)
	272 138.36	$6_{3,3,0} - 5_{3,2,0}$	86.73	6.0	254 (60)	−57.8 (0.3)	3.9 (0.9)	61 (13)
	272 417.25	$6_{2,4,0} - 5_{2,3,0}$	67.53	7.0	323 (72)	−58.0 (0.9)	4.6 (0.9)	66 (11)

Appendix B: Partition function of CH_3OD

Table B.1 gives the respective CH_3OD-A and CH_3OD-E rotation partition functions we use in the present study.

Table B.1. Rotational partition function for CH_3OD.

CH_3OD-A		CH_3OD-E	
T (K)	Q	T (K)	Q
9.375	18.1	9.375	15.5
18.75	52.3	18.75	50.8
37.5	153.5	37.5	153.2
75	458.6	75	458.6
150	1537.5	150	1537.1
225	3319.7	225	3316.7
300	5739.8	300	5727.9

Appendix C: IRAM-30m observations overlaid with our LTE modeling for $^{13}CH_3OH$, CH_3OD-A and CH_3OD-E

Figures C.1–C.3 show a montage of the detected $^{13}CH_3OH$, CH_2DOH, CH_3OD-A and CH_3OD-E transitions (see Tables A.3 and A.4 for the observational line parameters) along with our LTE modeling.

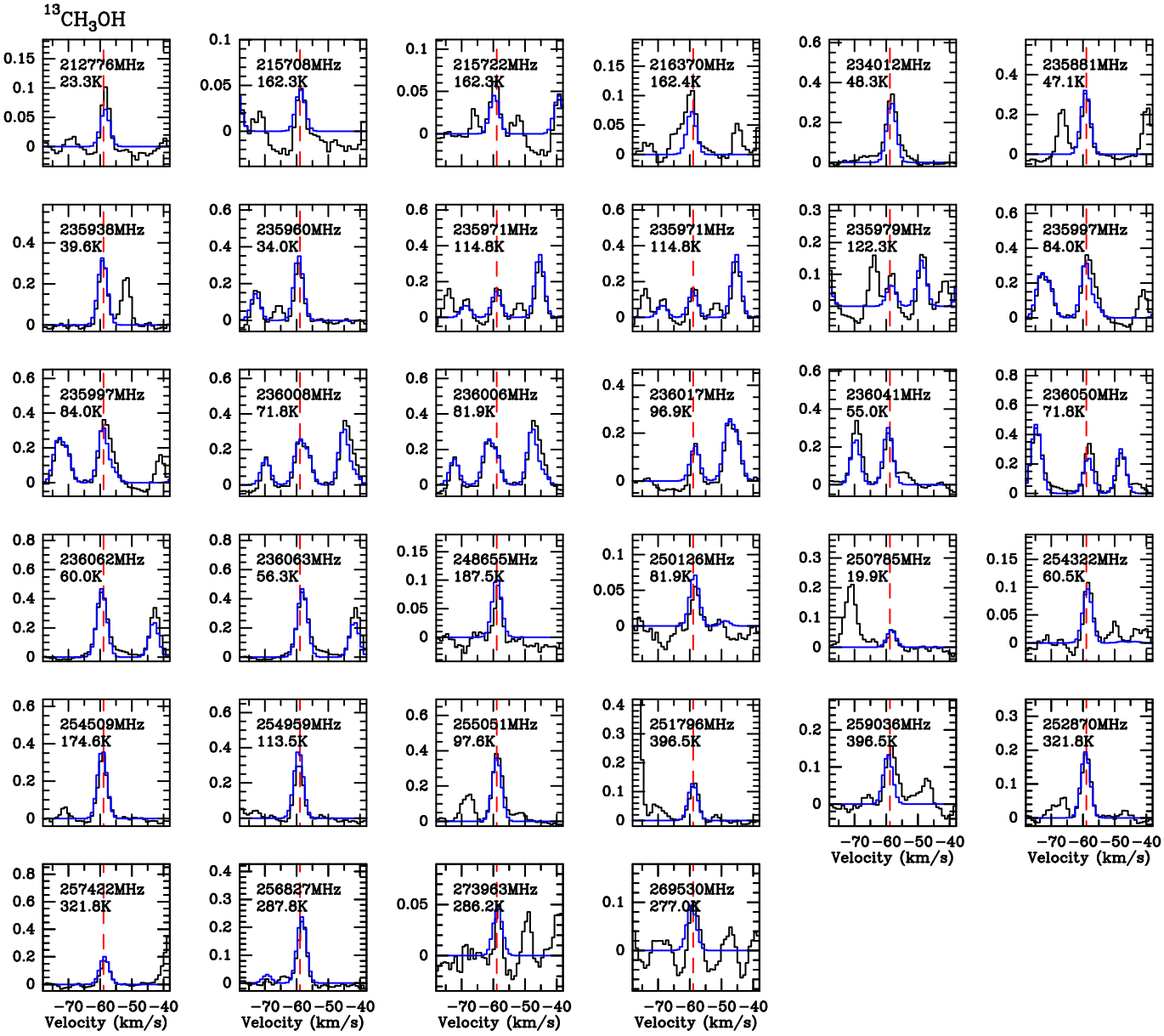

Fig. C.1. Montage of detected transitions associated with the methanol ^{13}C isotopolog towards NGC 7538-IRS1. Our LTE modeling is displayed in blue. Intensities are expressed in units of T_{mb}. The red dashed line marks the ambient cloud velocity $v_{LSR} = -58.9\,km\,s^{-1}$.

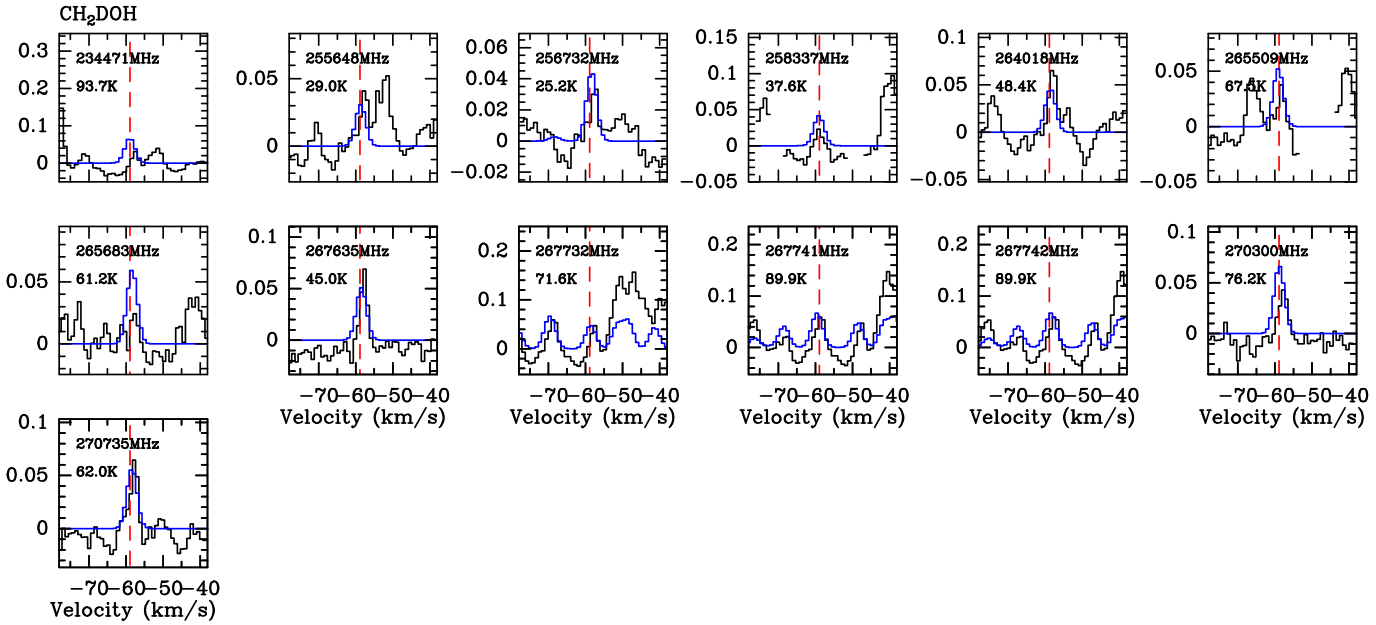

Fig. C.2. Montage of detected transitions associated with the deuterated CH_2DOH methanol towards NGC 7538-IRS1. Our LTE modeling is displayed in blue. Intensities are expressed in units of T_{mb}. The red dashed line marks the ambient cloud velocity $v_{LSR} = -58.9\,km\,s^{-1}$.

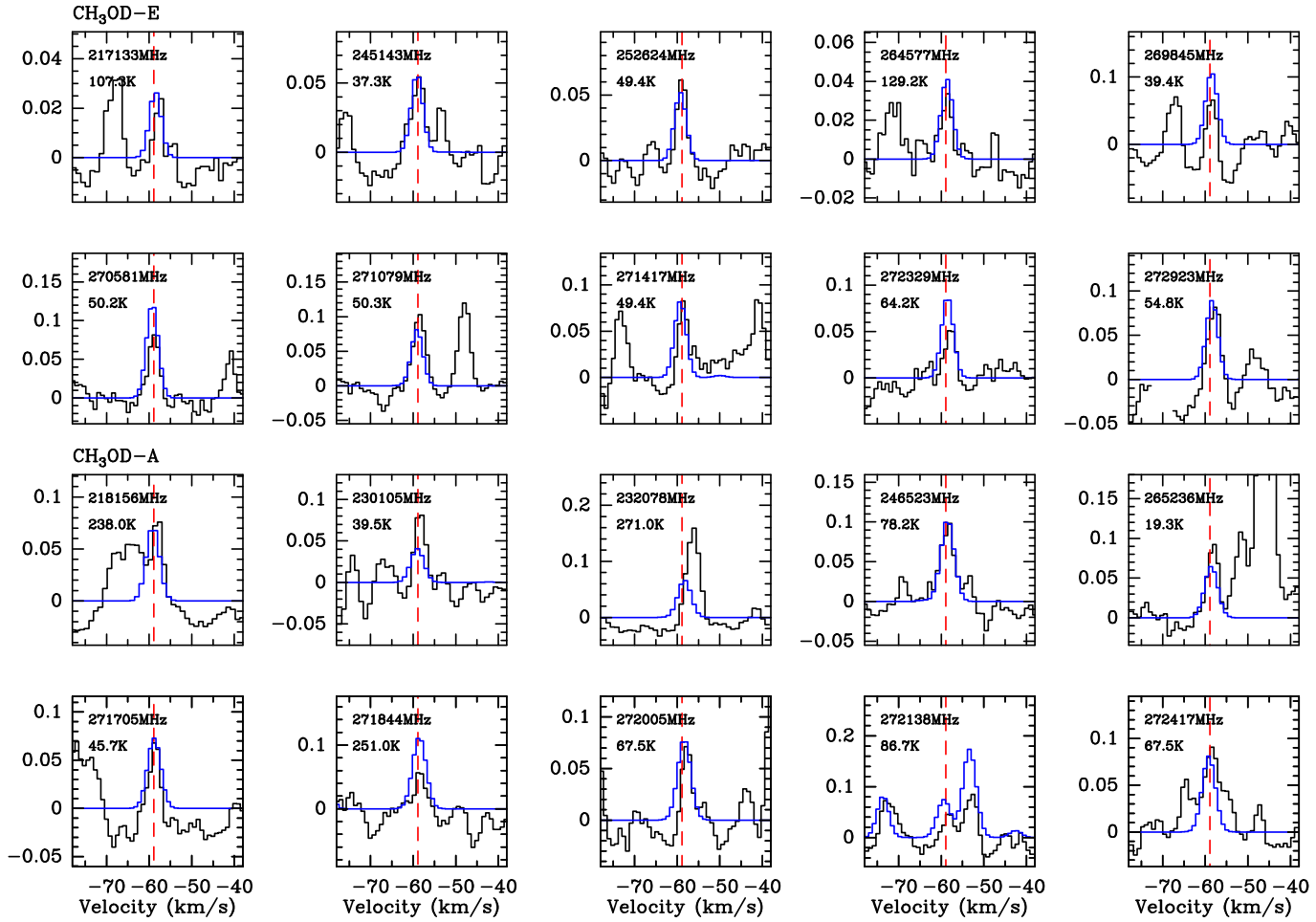

Fig. C.3. Montage of detected transitions associated with the CH_3OD, -A and -E forms towards NGC 7538-IRS1. Our LTE modeling is displayed in blue. Intensities are expressed in units of T_{mb}. The red dashed line marks the ambient cloud velocity $v_{LSR} = -58.9\,km\,s^{-1}$.